



Investigation of permanent magnet synchronous machines with buried magnets and carbon fiber sleeve for automotive application

Maximilian Clauer · Andreas Binder

Received: 28 November 2022 / Accepted: 15 February 2023
© The Author(s) 2023

Abstract Due to the limited space available in vehicles, traction drives with high torque densities are a key objective of machine design in the automotive sector. In order to be able to dispense with a multi-speed transmission and still achieve high vehicle end speeds, there is also the design objective of a high motor speed. Therefore, permanent magnet synchronous machines with buried magnets are preferred. In the following, a rotor concept is presented as a combination of buried rotor magnets and a carbon fiber sleeve in order to eliminate the radial and tangential rotor iron ribs. The resulting reduction in magnetic flux leakage, in combination with high mechanical strength, leads to an increased magnet utilization for the air-gap field and, thus, allows for a high torque density as well as high maximum speed. A disadvantage, however, is the increased manufacturing effort required for the production and assembly of the carbon fiber sleeve.

Keywords Automotive drives · High-speed drives · Carbon fiber sleeve · Permanent magnet synchronous machine with buried magnets · Comparison of rotor concepts

Untersuchung von Permanentmagnet-Synchronmaschinen mit vergrabenen Magneten und Kohlefaserbandage für Automobilanwendungen

Zusammenfassung Aufgrund des begrenzt zur Verfügung stehenden Bauraums in Fahrzeugen sind Traktionsantriebe mit hohen Drehmomentdichten ein wesentliches Ziel der Maschinenauslegung im Automobilsektor. Um auf ein Mehrganggetriebe verzichten zu können und dennoch hohe Fahrzeugendgeschwindigkeiten zu erzielen, besteht zudem das Auslegungsziel einer hohen Motordrehzahl. Bevorzugt werden daher permanentmagneterregte Synchronmaschinen mit vergrabenen Magneten eingesetzt. Im Folgenden wird ein Rotorkonzept als Kombination aus vergrabenen Rotormagneten und Kohlefaserbandage vorgestellt, um so die radialen sowie tangentialen Rotoreisenstege zu eliminieren. Die hierdurch erzielte Reduktion des Magnetstreufusses in Kombination mit einer hohen mechanischen Festigkeit führt zu einer erhöhten Magnetausnutzung für das Luftspaltfeld und erlaubt somit eine hohe Drehmomentdichte bei gleichzeitig hoher Maximaldrehzahl. Nachteilig ist allerdings ein erhöhter Fertigungsaufwand für die Herstellung und Montage der Kohlefaserbandage.

Schlüsselwörter Automobilantriebe · Hochdrehzahlantriebe · Kohlefaserbandage · Permanentmagnet-Synchronmaschine mit vergrabenen Magneten · Vergleich von Rotorkonzepten

M. Clauer (✉) · A. Binder
Institut für Elektrische Energiewandlung,
Technische Universität Darmstadt,
Landgraf-Georg-Str. 4, 64283 Darmstadt, Germany
mclauer@ew.tu-darmstadt.de

1 Introduction

The target of today's automakers in developing the powertrain of high-performance vehicles is high torque combined with high maximum speed. This

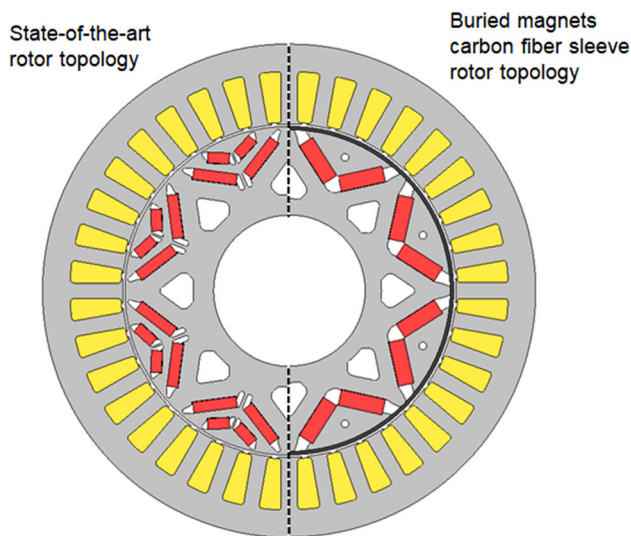


Fig. 1 Cross-section of a state-of-the-art rotor topology (left) and a buried magnets carbon fiber sleeve rotor topology (right)

enables both high acceleration of the vehicle and high top speed. Currently, preferably drives without multi-speed transmission are implemented in these vehicles. The main advantages of high-speed machines are the avoidance of transmission costs, losses and weight. In addition, noise can also significantly reduced by eliminating the need for an additional transmission.

With the *Model S Plaid*, *Tesla* is bringing a rotor concept with buried permanent magnets and carbon fiber sleeve into series production, for the first time. The concept differs from current rotor topologies mainly by the omission of the iron ribs in the rotor [1], which are undesirable from an electromagnetic point of view, but necessary for the mechanical stability of this specific topology [2, 3].

In the following, a designed machine with buried permanent magnets and carbon fiber sleeve is described and the main influence of the rotor concept is analyzed from the electromagnetic point of view. The mechanical and electromagnetic design of such a machine is then presented. Subsequently, the rotor concept is compared with a state-of-the-art rotor topology (Fig. 1) and the specific advantages and disadvantages are contrasted.

2 Analysis of rotor concept

The designed machine has a peak power of 130 kW and a peak torque of 270 Nm at a rotor as well as a stator temperature of 100 °C. The maximum feasible speed is 15000 min⁻¹. Figure 2 shows the exploded view of the rotor with buried permanent magnets in a V-shape arrangement, which are fixed with a pre-stressed carbon fiber sleeve.

The electric machine is designed as a three-phase eight pole interior permanent magnet synchronous machine (IPMSM) with a round wire fractional slot winding. The number of slots per pole and phase is 3/2, which leads to 36 semi-closed slots in the stator. The distributed two-layer winding within the slots is 8/9-short pitched. Due to the fractional slot winding, the machine has lower cogging torque at no-load and torque ripple under load compared to an integer slot winding. Figure 3 shows the cross-section of the machine.

The concept that combines buried permanent magnets with a carbon fiber sleeve aims to eliminate the radial and tangential rotor iron ribs, and therefore the magnetic flux leakage of the magnets. The flux barriers extend to the outer diameter of the rotor so that the carbon fiber sleeve holds the magnets and the upper iron stacks in place at high centrifugal forces. The rotor also consists of lightening holes in the lower iron stack to reduce mass and moment of inertia of the rotor. Figure 4 shows the no-load condition simulated by finite element analysis (FEA) using the software *JMAG 20*.

By eliminating the radial and tangential rotor iron ribs, a significant reduction in magnetic flux leakage, and thus high magnet utilization is achieved. However, the increased total air-gap, consisting of the mechanical air-gap width and the carbon fiber sleeve height, counteracts the magnetic flux gain, because the magnetic resistance is higher compared to a pure mechanical air-gap. The main data of the designed machine are listed in Table 1.

3 Mechanical design and calculation

Sufficient mechanical stability is a prerequisite for the subsequent electromagnetic design. In order to design the carbon fiber sleeve, an analytical calculation

Fig. 2 Exploded view of the rotor with buried permanent magnets and carbon fiber sleeve (Inventor 2020)

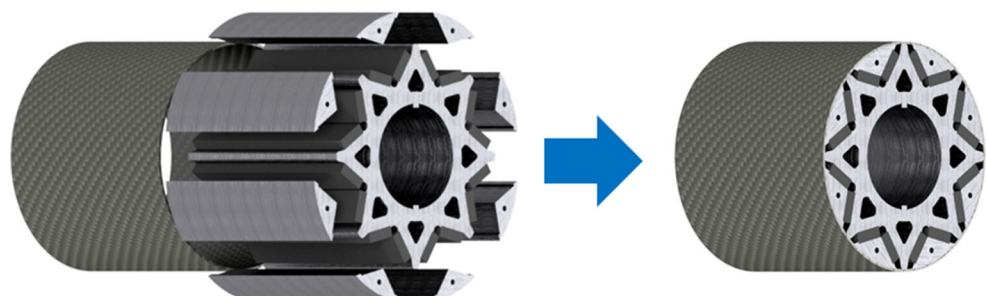
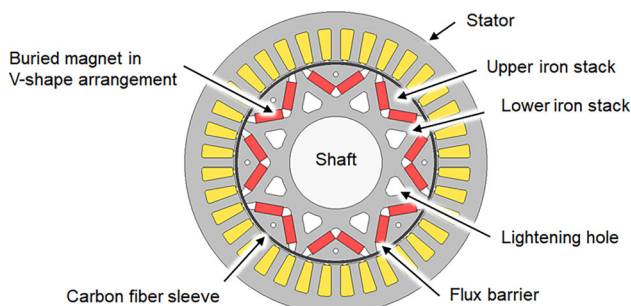
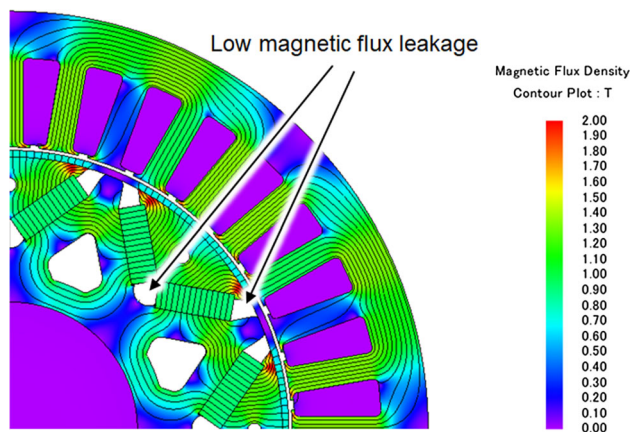


Table 1 Main design data of the IPMSM

Parameter	Symbol	Value	Parameter	Symbol	Value
Number of phases	m	3	Total air-gap width	δ_{eff}	2.1 mm
Number of poles	$2p$	8	Magnet V-angle	α_{pm}	110°
Number of slots	Q	36	Magnet segment height	h_{pm}	5.8 mm
Number of slots per pole and phase	q	3/2	Magnet segment width	b_{pm}	16.5 mm
Short pitch	W/τ_p	8/9	Magnet segment length	l_{pm}	27.5 mm
Number of parallel winding branches per phase	a	4	Copper fill factor	k_{Cu}	44.4%
Number of strands per turn	a_t	5	Total axial length	L	213.0 mm
Number of turns per phase	N_s	42	Total outer diameter	D	215.0 mm
Outer diameter of the stator iron stack	d_{so}	180.0 mm	Total machine volume	V	7.73 dm ³
Inner diameter of the stator iron stack	d_{si}	121.5 mm	Permanent magnet mass	m_{pm}	1.3 kg
Axial iron length of the iron stack	l_{fe}	110.0 mm	Iron stack mass	m_{fe}	12.9 kg
Air-gap width	δ_m	0.7 mm	Copper mass	m_{Cu}	3.8 kg
Carbon fiber sleeve height	h_s	1.4 mm	Total active mass	m_{act}	18.0 kg

**Fig. 3** Cross-section of the rotor concept with buried permanent magnets and carbon fiber sleeve (JMAG 20)**Fig. 4** Simulated field distribution and flux density at no-load condition at a permanent magnet temperature of $\theta_{\text{pm}} = 100^\circ\text{C}$ by means of a FEA (JMAG 20)

of the required sleeve height and undersize is performed.

The calculation takes the material properties of carbon fiber into account and therefore the sleeve is modelled as an orthotropic thick shell according to [4]. The thermal expansion under load and the pre-stress are the dominating effects on the sleeve. The centrifugal force loading of the sleeve by the permanent magnets and the upper iron stack does not matter, as

long as the sleeve still exerts a positive preload on the rotor. This condition must always be satisfied during the design of the sleeve. For simplicity, the buried permanent magnets and the iron laminations of the rotor are modelled using an equivalent hollow cylinder arrangement. Additionally, contact force due to the glue is neglected in the following model. Since the mass densities of the iron laminations ($\rho_{\text{fe}} = 7630 \text{ kg/m}^3$) and the permanent magnets ($\rho_{\text{pm}} = 7550 \text{ kg/m}^3$) as well as the E -modules ($E_{\text{fe}} = 196 \text{ GPa}$, $E_{\text{pm}} = 200 \text{ GPa}$) are quite similar, the material properties of iron laminations are used in the model. The thermal expansion coefficient of the equivalent hollow cylinder arrangement is determined through the mass ratio of the permanent magnets and the iron laminations. The applied simplified model considered the influence of:

- Load due to the pre-stress of the sleeve (press fit)
- Load due to the additional expansion during rotor heating
- Load due to the elongation of the sleeve by the centrifugal force

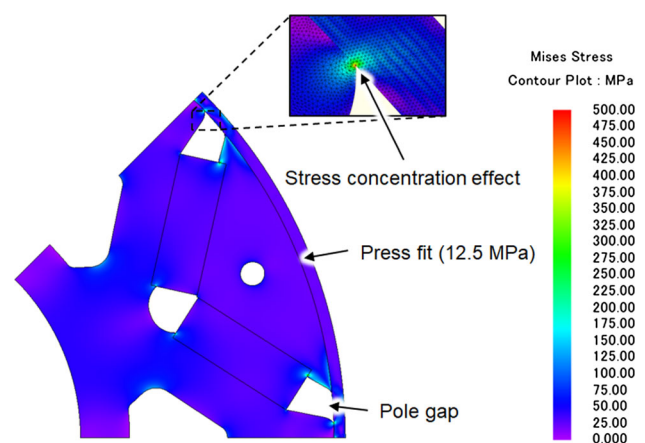
**Fig. 5** Simulated stress concentration effect due to the pole gaps, with an element size of 0.06 mm at standstill $n=0 \text{ min}^{-1}$ and a press fit of 12.5 MPa (JMAG 20)

Table 2 Material data of the IPMSM at a temperature of 20 °C (r , φ and z are spatial directions in the cylindrical coordinate system, due to orthotropic material properties of the carbon fiber, (–) denotes compressive and (+) denotes flexural strength)

Material (Component)	M270-35A (Iron laminations)	31CrMo9 (Shaft)	BMN-42EH/S (Magnet)	60% HTS 5631 matrix (Carbon fiber sleeve)
R_m /MPa	555	1000	(–) 1000 / (+) 90	2615 (φ) / 90 (r)
$R_{p0.2}$ /MPa	440	800	–	–
ρ /(kg/m ³)	7630	7750	7550	1550
E /GPa	196	210	200	145.28 (φ)/12 (rz)
ν	0.3	0.3	0.3	0.278 ($r\varphi$)/0.023 (φz)/0.388 (rz)
α /K ^{–1}	$12.03 \cdot 10^{-6}$	$12.1 \cdot 10^{-6}$	$3.0 \cdot 10^{-6}$	$34.3 \cdot 10^{-6}$ (φ) / $0.14 \cdot 10^{-6}$ (r)

By assuming a non-compressible rotor shaft, iron stacks and permanent magnets the elongation is equal to the applied undersize of the sleeve. From this, the resulting sleeve pressure can be determined via the expansion of a cylinder under internal pressure. The rotor heating that occurs during operation leads to an expansion of the rotor shaft as well as the iron laminations (including permanent magnets). This increases the undersize of the sleeve, since the coefficient of thermal expansion of carbon fibers in the radial direction is negligible. Likewise, the inherent mass of the sleeve leads to additional elongation due to the centrifugal force. This increases the mechanical stress load on the sleeve, whereby the undersize is reduced. Due to the pole gaps of the rotor design, additional mechanical stress occurs in the sleeve [5]. Figure 5 shows the stress concentration effect of a pre-stressed carbon fiber sleeve ($p_c = 12.5 \text{ N/mm}^2$) at standstill $n = 0 \text{ min}^{-1}$ by means of a two-dimensional FE-calculation.

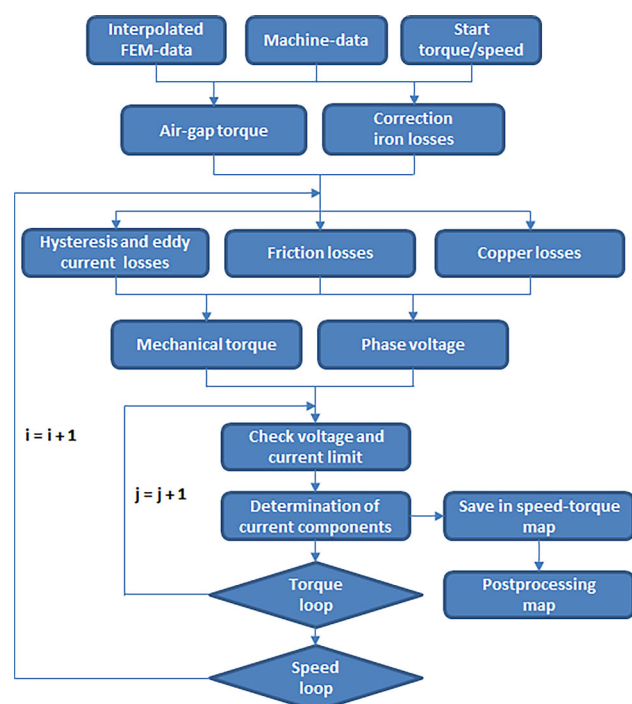
The occurring stress concentration effect in the sleeve due to the pole gaps, are taken into account in a safety factor. As carbon fiber material is very sensitive to bending forces, a thin layer of glass fiber at the inner of the sleeve is recommended to reduce this effect [5]. The proper rounding of the edges, which are in contact with the sleeve, also reduces the stress concentration effect. Imperfections during the manufacturing process, such as resin accumulation or air pockets, can lead to a deterioration of the mechanical properties of the sleeve [6]. In addition, the mechanical properties depend on the temperature. As temperature increases, mechanical properties also deteriorate [5]. This knowledge is taken into account in additional safety factors. The overall safety factor S for the sleeve design consists of:

- Manufacturing influence $S_m = 2.0$
- Temperature influence $S_\theta = 1.1$
- Stress concentration influence $S_s = 2.2$

The applied overall safety factor is therefore $S = 4.8$. Hence, the maximum permissible mechanical stress in fiber direction (φ) of the sleeve is $\sigma_{\varphi, \text{lim}} = 545 \text{ N/mm}^2$. For the design, a maximum temperature of $\theta_{\text{pm}} = 120^\circ \text{C}$ for the rotor is assumed and taken into account. According to the IEC 60034-1 standard, the rotor must withstand 1.2 times the maximum speed

for 2 min. In this case the applied over-speed is $n_{\text{os}} = 18000 \text{ min}^{-1}$, which leads to a rotor circumferential speed of $v_u = 113 \text{ m/s}$. During this condition, the sleeve must provide a positive residual contact pressure p_c between the magnets and the rotor iron stack, whereby the maximum permissible stress in fiber direction inside the sleeve is not exceeded. The material data for the calculations are set according to Table 2.

With respect to the electromagnetic performance of the machine, the carbon fiber sleeve height is selected to $h_s = 1.4 \text{ mm}$ and the undersize to $u_v = 220 \mu\text{m}$. This results in residual contact pressure at over-speed and 20°C rotor temperature of $p_c = 12.5 \text{ N/mm}^2$ as a worst-case scenario. The maximum stress in fiber direction (φ) is calculated at over-speed and maximal rotor temperature of $\theta_{\text{pm}} = 120^\circ \text{C}$ to $\sigma_{\varphi, \text{max}} = 544.9 \text{ N/mm}^2$. As this is below the applied overall safety factor and the contact pressure is still positive, the rotor is assumed to be mechanically stable.

**Fig. 6** Flowchart of the calculation process for the efficiency-optimized map within the speed-torque range [7]

To mount the sleeve, it is possible to cool the rotor with liquid nitrogen to a temperature of -190°C . The thermal shrinkage of the rotor causes the sleeve to be mounted on the rotor without axial pressure. The expansion of the rotor during the thermal adjustment to room temperature generates the preload.

4 Electromagnetic design and calculation

The basis of the electromagnetic calculation process is a parametric two-dimensional finite element (FE) model of the IPMSM, which is created in the com-

mercial FE software *JMAG 20*. The parametric model enables a variation of the stator and rotor topology as well as the machine geometry. Figure 6 shows the semi-analytical calculation procedure for a efficiency-optimized operation at sinusoidal current injection [7].

The parameter identification within the $6 \times 6 \hat{I}_d\text{-}\hat{I}_q$ -Grid and subsequent spline interpolation is performed at a reference speed of $n_{\text{sim}} = 4244 \text{ min}^{-1}$. Scaling factors are used to adjust for different electrical frequencies within the speed loop. For the hysteresis losses in the iron laminations, $k_{\text{fe,hys}} = 1$ and for

Fig. 7 Result of the DoE with 110 machine designs

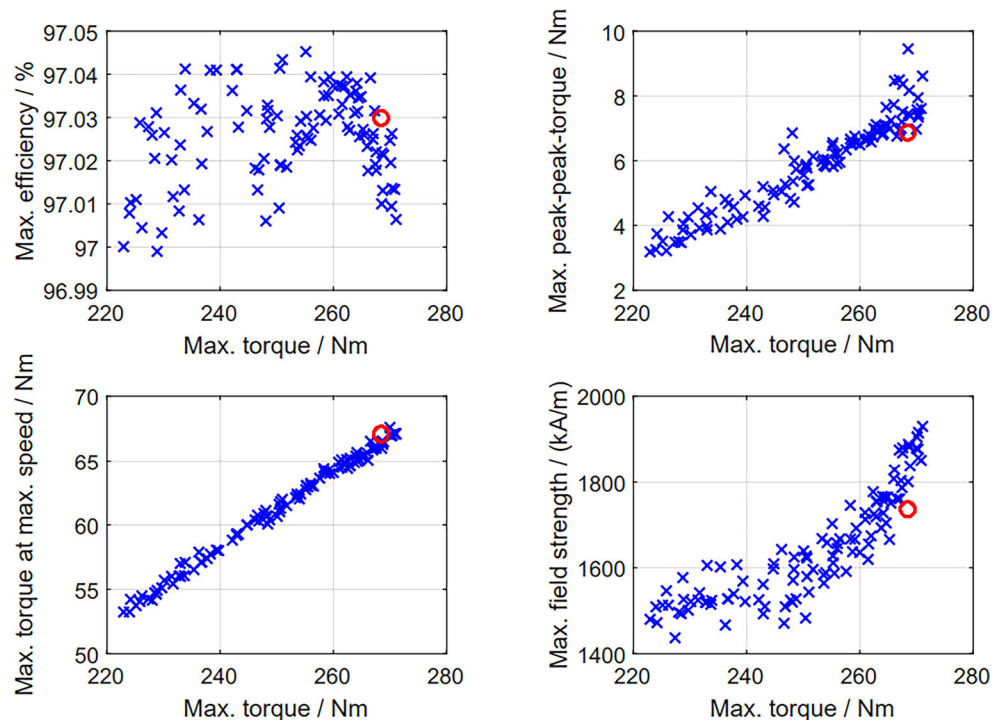
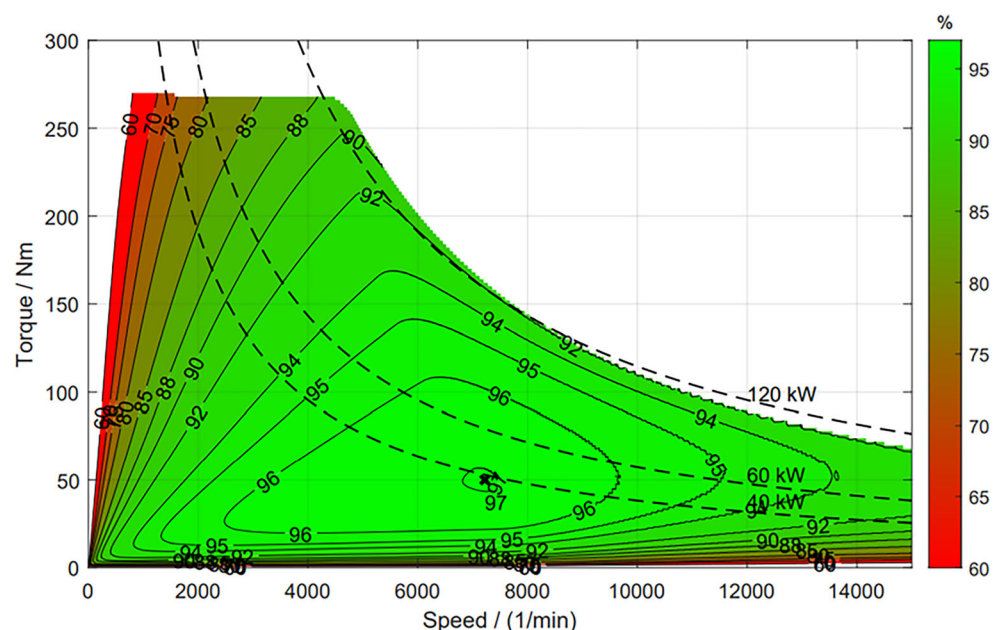


Fig. 8 Calculated efficiency-optimized map at sinusoidal current injection for a permanent magnet and winding temperature of $\vartheta_{\text{pm}} = \vartheta_{\text{cu}} = 100^{\circ}\text{C}$, max. RMS stator voltage of $U_{\text{s,lim}} = 230 \text{ V}$, max. stator RMS current of $I_{\text{s,lim}} = 300 \text{ A}$, and iron loss increase factor of $k_{\text{d,fe}} = 1.5$



the eddy currents in the iron laminations as well as in the permanent magnets, $k_{fe,eddy} = k_{pm,eddy} = 1.6$ is applied.

Due to the manufacturing process of the iron laminations, an additional iron loss increase factor $k_{d,fe} = 1.5$ is included in the calculation. The increased resistance factor $k_{d,cu}$ due to first and second order current displacement as well as the friction losses are calculated analytically. The mention correction and loss increase factors are determined by the fitting of the simulation data with the measured data of a similar machine. Because of the same applied materials, these factors are also used in the simulation of the IPMSM with sleeve.

A permanent magnet and a stator winding temperature of $\vartheta_{pm} = \vartheta_{cu} = 100^\circ\text{C}$, a DC-link voltage of $U_{DC,lim} = 600\text{ V} < U_{DC,n} = 800\text{ V}$ and a stator RMS current of $I_{s,lim} = 300\text{ A}$ are used as boundary conditions for the selection of the operating points. A high-energy neodymium-iron-boron material BMN-42EH/S from the company *Bomatec* is used as the permanent magnets, with a remanence of $B_{r,100^\circ\text{C}} = 1.12\text{ T}$ and a coercivity of the magnetic polarization of $H_{cJ,100^\circ\text{C}} = 1434\text{ kA/m}$ at a temperature of $\vartheta_{pm} = 100^\circ\text{C}$. Due to the rather low electrical conductivity of carbon fiber material, which is in the range of $\kappa_s = 3 \cdot 10^4\text{ S/m}$ [8, 9], the eddy current losses within the sleeve are negligible small [10] and therefore not included in the electro-magnetic calculation.

For a fair evaluation of the rotor concept, the stator of the designed machine is taken from an already built and measured prototype machine. Therefore, the stator geometry and winding configuration is fixed during the optimization process. For reasons of comparability, the mass of the permanent magnets is also fixed to $m_{pm} = 1.3\text{ kg}$.

For the design of experiment (DoE) with latin hypercube sampling, both the initial parameter con-

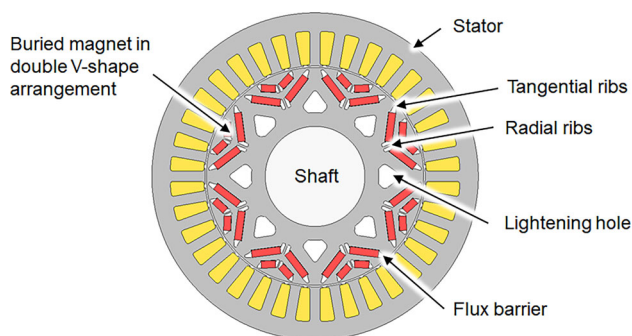


Fig. 9 Cross-section of the manufactured and measured prototype IPMSM without sleeve (JMAG 20)

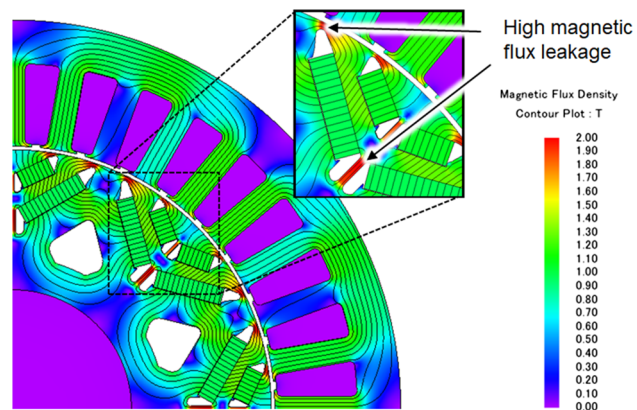


Fig. 10 Simulated magnetic field distribution and flux density at no-load condition at a permanent magnet temperature of $\vartheta_{pm} = 100^\circ\text{C}$ (JMAG 20)

straints and the parameter ranges of the optimization are specified. Figure 7 shows the results of the parameter variation.

The red circle marks the finally selected machine design. Figure 8 shows the calculated efficiency-optimized map for the machine with sinusoidal current injection.

5 Comparison of IPMSM with and without carbon fiber sleeve

For a comprehensive evaluation of the concept, the IPMSM with sleeve is compared to a manufactured

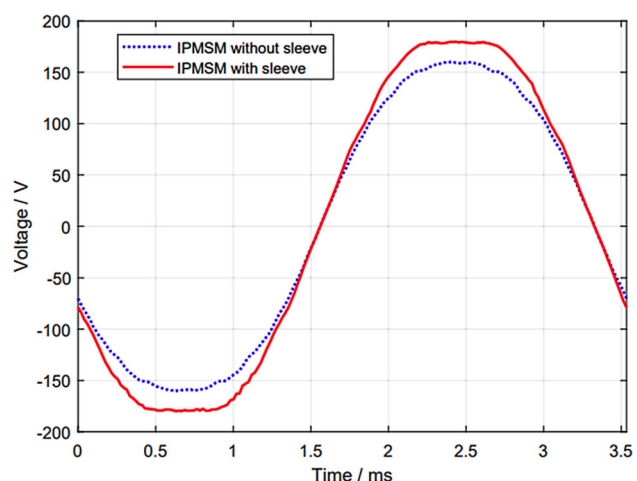
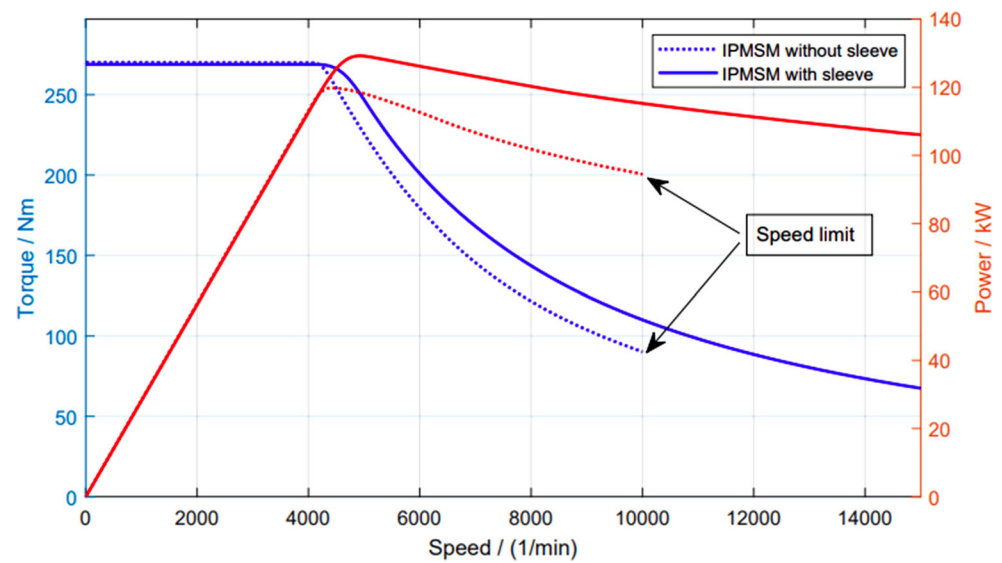


Fig. 11 Comparison of simulated no-load voltage in phase U for one electrical period at the speed of $n = 4244\text{ min}^{-1}$ and the permanent magnet temperature of $\vartheta_{pm} = 100^\circ\text{C}$

Table 3 Specific data of the manufactured prototype IPMSM without sleeve

Parameter	Symbol	Value	Parameter	Symbol	Value
Air-gap width	δ_m	0.8 mm	Magnet segment height 1./2. layer	h_{pm}	4.0 mm
Magnet V-angle 1. layer	α_{pm1}	120°	Magnet segment width 1./2. layer	b_{pm}	8.0 mm
Magnet V-angle 2. layer	α_{pm2}	130°	Magnet segment length 1./2. layer	l_{pm}	27.5 mm

Fig. 12 Comparison of calculated limit characteristics at a permanent magnet and winding temperature of $\vartheta_{pm} = \vartheta_{cu} = 100^\circ\text{C}$, max. RMS stator voltage of $U_{s,lim} = 230\text{V}$ and max. stator RMS current of $I_{s,lim} = 300\text{A}$



and measured prototype machine with buried permanent magnets and radial as well as tangential rotor iron ribs. The prototype machine has a peak power of 120kW and a peak torque of 270Nm at a rotor as well as a stator temperature of 100°C . The maximum feasible speed is 10000min^{-1} . Due to iron ribs, the rotor withstands centrifugal forces at the required overspeed of $n_{os} = 12000\text{min}^{-1}$ with a safety factor of $S = 1.6$ with respect to the yield strength $R_{p0.2}$ of the iron laminations. Figure 9 shows the cross-section of the state-of-the-art IPMSM without sleeve.

The specific rotor data are given in Table 3, whereby the stator topology remains the same as listed in Table 1.

If the permanent magnets are buried within the rotor laminations, the rotor iron itself holds the magnets in place. Thus, no carbon fiber sleeve is necessary and

total air-gap is reduced. The air-gap width of the machine is $\delta_m = 0.8\text{mm}$ and thus the magnetic resistance of the air-gap is 62% smaller compared to the IPMSM with sleeve, whereby the relative magnetic permeability of the carbon fiber material is set to $\mu_{r,s} = 1$ [5]. However, this design leads to a massive leakage flux of the permanent magnets and counteracts the lower magnetic resistance. Figure 10 shows the simulated no-load condition.

The plotted no-load voltage of the phase U in Fig. 11 shows, that the machine design without carbon fiber sleeve has a slightly lower value, and thus a lower magnetic flux linkage due to the massive leakage.

Figure 12 shows the limit characteristics of the IPMSM with and without sleeve for the given boundary conditions of a permanent magnet and winding temperature of $\vartheta_{pm} = \vartheta_{cu} = 100^\circ\text{C}$, a maximum RMS stator voltage of $U_{s,lim} = 230\text{V}$ and a maximum stator RMS current $I_{s,lim} = 300\text{A}$.

The juxtaposition indicates that the IPMSM with sleeve has a better field-weakening capability, while the maximum torque is quite similar. Whereby, previous work has shown that the optimum field weakening capability depends on the saliency ratio L_q/L_d and magnetic flux linkage Ψ_{pm} of the machine design [11].

Table 4 Comparison of machine characteristics

	IPMSM without carbon fiber sleeve	IPMSM with carbon fiber sleeve
Max. power/kW	120.0	129.8 (+8.2%)
Max. torque/Nm	269.5	268.4 (−0.4%)
Max. speed/ min^{-1}	10000	15000 (+50.0%)
Max. efficiency/%	96.9	97.0 (+0.1%)
Max. torque ripple/Nm	8.5	6.9 (−18.8%)

Table 5 Comparison of machine losses at different operating points (M1 denotes IPMSM without sleeve and M2 denotes IPMSM with sleeve)

Operating point	OP1 40 Nm, 3000 min^{-1}		OP2 40 Nm, 10000 min^{-1}		OP3 270 Nm, 4244 min^{-1}	
Machine	M1	M2	M1	M2	M1	M2
I^2R/W	332.0	316.2	845.6	968.8	15130.3	15294.9
Rotor iron/W	9.5	1.0	67.9	11.6	80.5	17.1
Stator iron/W	184.8	179.0	560.0	564.4	799.2	740.7
PM eddy current/W	1.2	0.3	15.0	3.7	32.6	2.6
Friction/W	12.1	12.2	102.3	102.8	19.8	19.9
Total/W	539.6	508.7	1590.8	1651.3	16062.4	16075.1

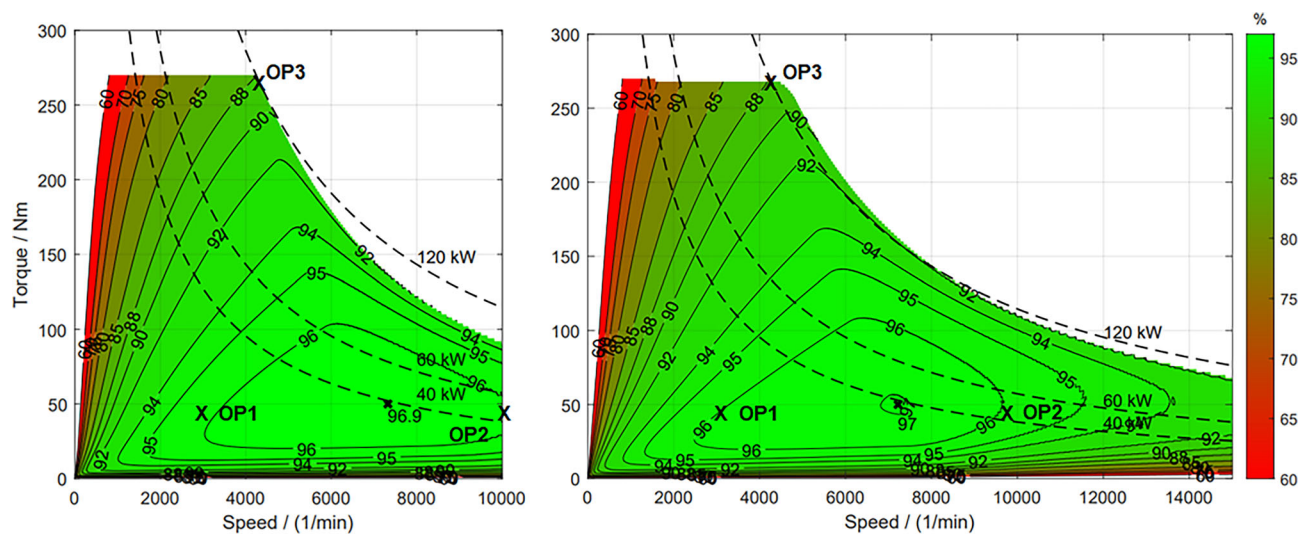


Fig. 13 Comparison of calculated efficiency for the IPMSM without sleeve (left) and with sleeve (right)

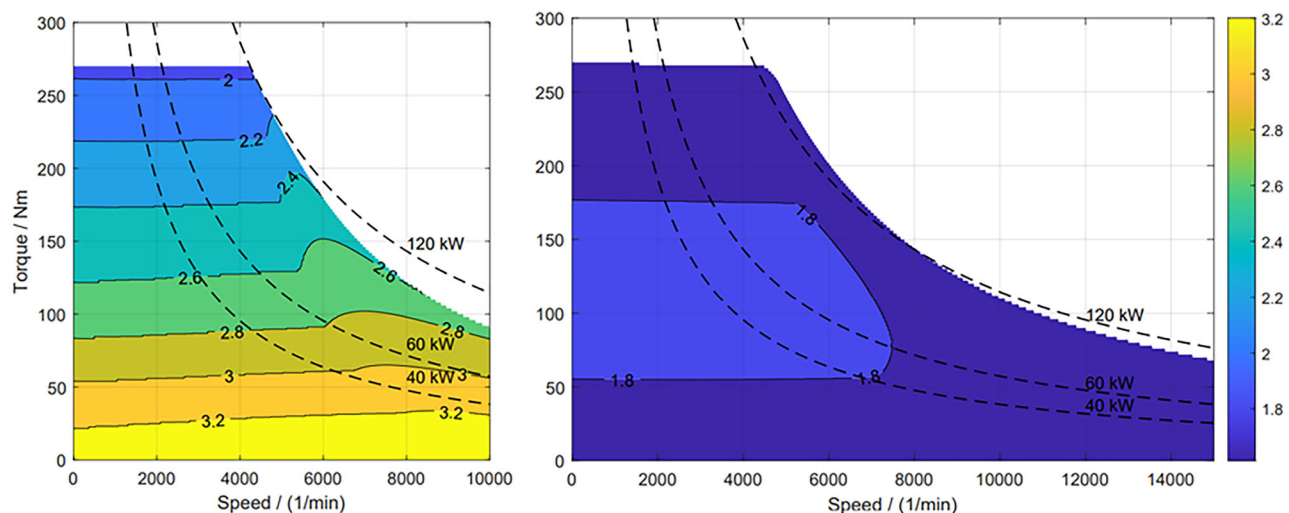


Fig. 14 Comparison of calculated saliency ratio for the IPMSM without sleeve (left) and with sleeve (right)

Table 4 gives an overview of the main characteristics of the two machines.

The comparison shows that the IPMSM with sleeve maintains the maximum torque and efficiency while increasing the maximum speed (+50.0%) as well as the power (+8.2%) and minimize the torque ripple under load at the same time. Figure 13 shows the simulated efficiency maps of both machines.

Table 5 lists the separate losses at three different operating points, which are also marked in Fig. 13.

At low speed and low torque (OP1) the effect of the higher magnet utilization and the saliency ratio of the IPMSM with sleeve, reduce the dominant I^2R -losses (-4.8%). While at high speed and low torque (OP2), this leads to higher I^2R -losses (+14.5%). At the maximum power (OP3) the total losses are quite similar, with increased I^2R -losses and reduced iron losses. This is due to the very different rotor structure and

thus magnetic paths of the two machines. Figure 14 shows the saliency ratio of both machines.

The juxtaposition shows, that the IPMSM without sleeve and with iron ribs exhibits a strong decrease in saliency at higher torque and thus a strong dependence on iron saturation. On the other hand, the IPMSM with sleeve has a quite equal saliency ratio over the entire operating points. This also leads to a very different utilization of the reluctance torque for a minimal loss operation. Figure 15 shows the percentage share in reluctance torque in both machines.

With up to 60% reluctance torque, the IPMSM without sleeve generates a higher amount of reluctance torque over the entire operating points.

To reduce the eddy current losses in the conductive permanent magnets, the lower layer in the IPMSM without sleeve is divided into two segments in circumferential direction. For further examinations of the losses, Fig. 16 shows the total rotor losses, con-

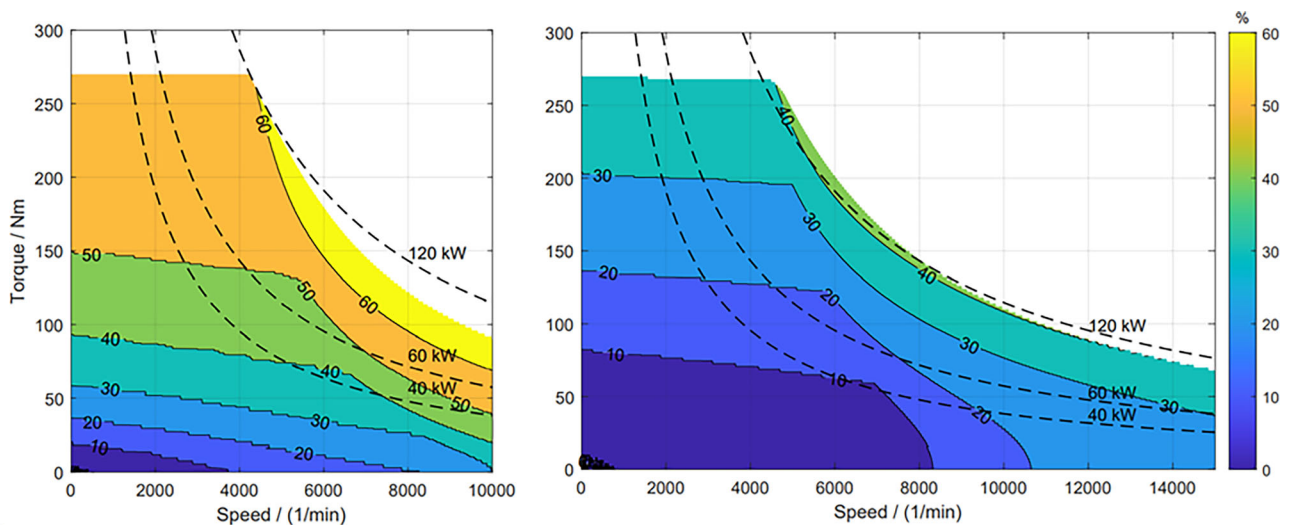


Fig. 15 Comparison of calculated percentage share in reluctance torque for the IPMSM without sleeve (*left*) and with sleeve (*right*)

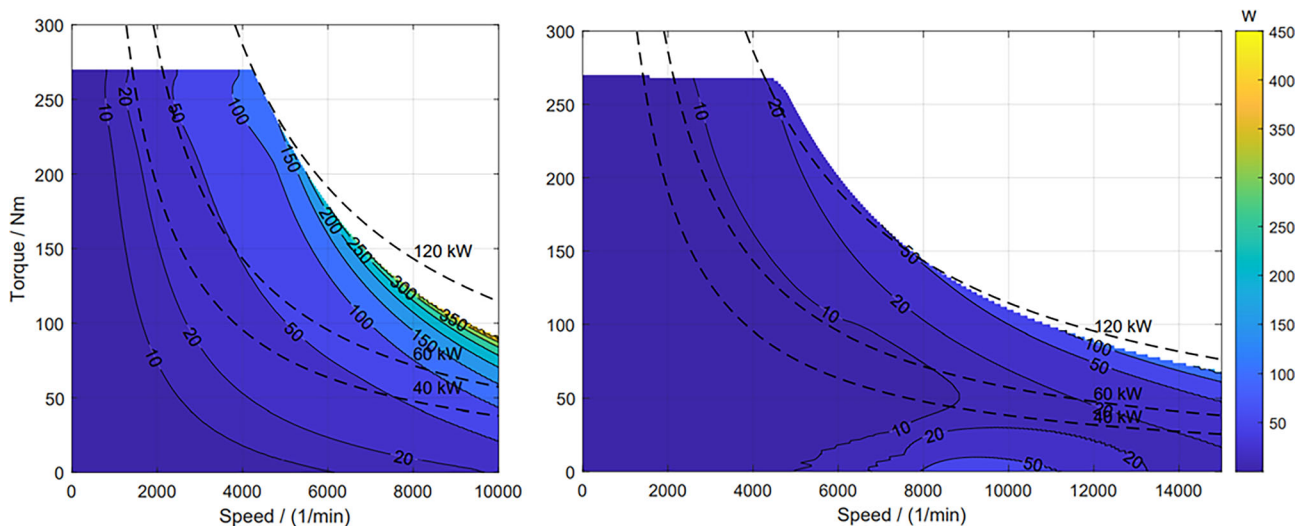


Fig. 16 Comparison of calculated total rotor loss for the IPMSM without sleeve (*left*) and with sleeve (*right*)

sisting of iron losses and eddy current losses within the permanent magnets, of the two machines.

Due to the higher magnetic resistance of the total air-gap of the IPMSM with sleeve, the losses within the rotor are smaller compared to the IPMSM without sleeve. Therefore, to use a larger air-gap is a very effective approach to reduce the space harmonic losses within the rotor [12, 13] and no additional magnet segmentation is necessary. The higher total air-gap also affects the cogging torque at no-load and the torque ripple under load [14]. In Fig. 17 the cogging torque at no-load for one electrical period of both machines is depicted.

Figure 18 shows the peak-to-peak torque ripple under load for both machines.

Although the IPMSM without sleeve shows a lower cogging torque at no-load, the maximum torque ripple under load is higher compared to the IPMSM with sleeve. Whereby, an axial two-step skewed rotor with

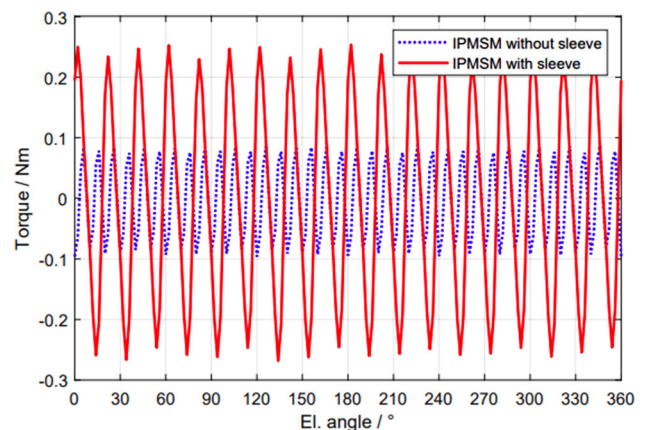


Fig. 17 Comparison of simulated cogging torque at no-load of one electrical period for both machines with a step size of 2° el

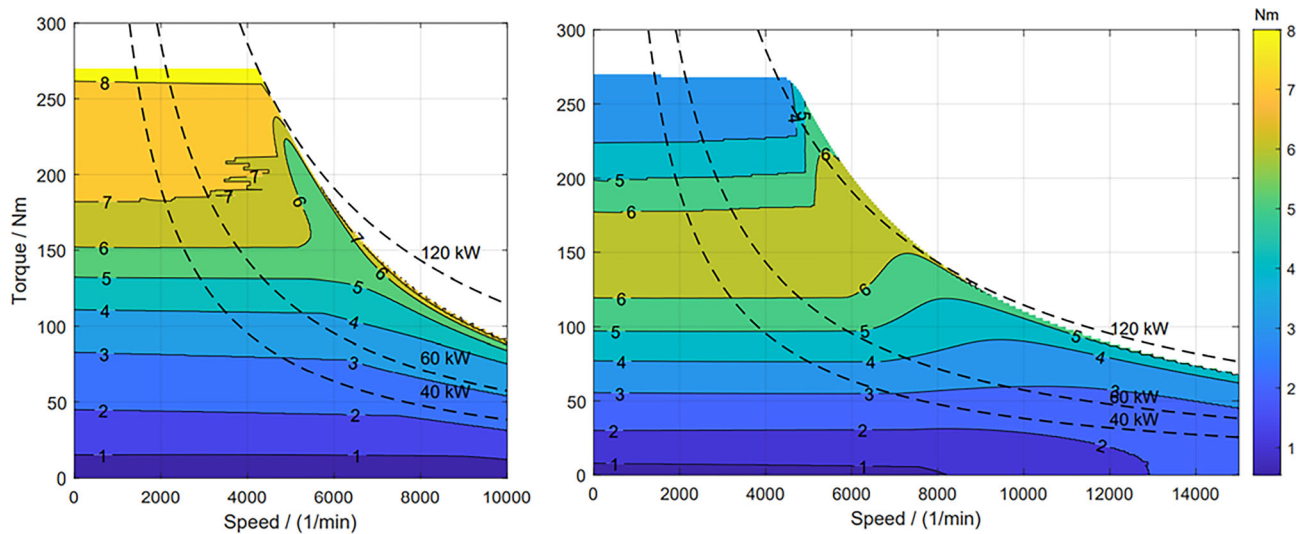


Fig. 18 Comparison of calculated peak-to-peak torque for the IPMSM without sleeve (*left*) and with sleeve (*right*)

a mechanical angle of 2.5° between the two rotor segments is used for the IPMSM without sleeve, in order to reduce the cogging torque at no-load and the torque ripple under load. Thus, no rotor step skew is necessary for the IPMSM with sleeve.

To avoid any risk of electromagnetic performance degradation, the irreversible demagnetization during an active short circuit, as a fail-safe operation, has to be considered. During this event, a high opposing magnetic field is generated in the permanent magnets, since there are no stray paths for the magnetic flux in the IPMSM with sleeve. Figure 19 shows the magnetic field distribution and flux density during an active short circuit event under the worst-case load condition (voltage zero crossing).

The maximum field strength applied on the magnetic material during the active short circuit is

$|H_{pm,max}| = 1736.4 \text{ kA/m}$. This is much higher (+54.8%) compared to the maximum field strength in the IPMSM without sleeve. Figure 20 shows the field strength within the permanent magnets plotted against time during the active short circuit event.

Depending on the rotor temperature, this could lead to an irreversible demagnetization of the permanent magnets. Figure 21 shows the comparison of the calculated thermal behavior of the permanent magnet and winding temperature.

The applied lumped parameter thermal network model is created in *Matlab/Simulink 20*. Whereby the same cooling system, consisting of a water cooling jacket, is used.

Because of the significant lower rotor losses on the applied operating point, the permanent magnet temperature of the IPMSM with sleeve is lower, al-

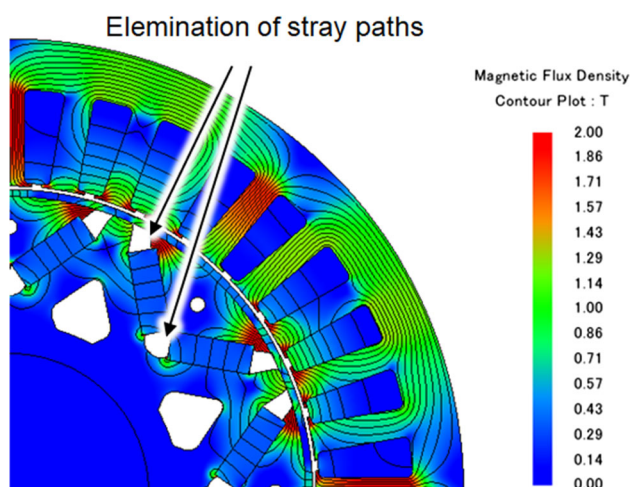


Fig. 19 Simulated magnetic field distribution and flux density during worst-case load condition for active short circuit with initial RMS stator current of $I_s = 300 \text{ A}$, current angle of $\beta_1 = -38.8^\circ$, and speed of $n = 4244 \text{ min}^{-1}$ at a permanent magnet and winding temperature of $\theta_{pm} = \theta_{cu} = 100^\circ \text{C}$ (JMAG 20)

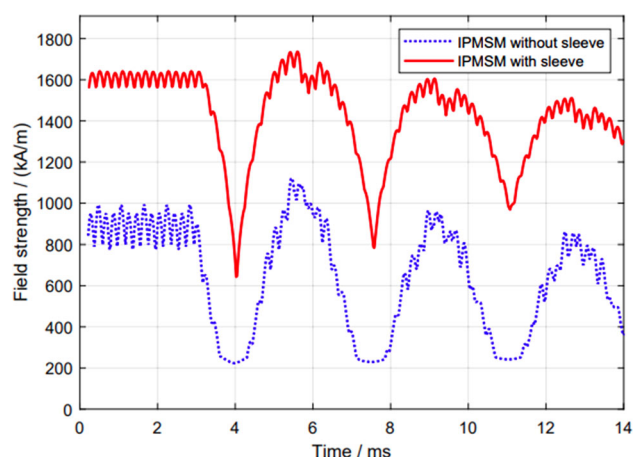


Fig. 20 Simulated field strength within the magnets during worst-case load condition for active short circuit with initial RMS stator current of $I_s = 300 \text{ A}$, current angle of $\beta_1 = -38.8^\circ$, and speed of $n = 4244 \text{ min}^{-1}$ at a permanent magnet and winding temperature of $\theta_{pm} = \theta_{cu} = 100^\circ \text{C}$

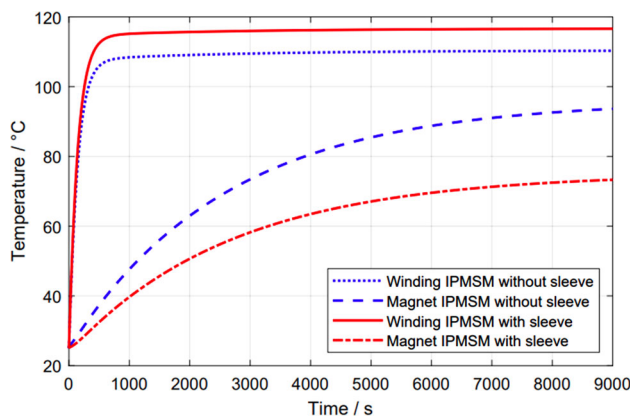


Fig. 21 Calculated temperature curves for both machines at a power of $P_{\text{mech}} = 40 \text{ kW}$ and speed of $n = 4244 \text{ min}^{-1}$ with a coolant temperature of $\vartheta_c = 40^\circ\text{C}$, an ambient temperature of $\vartheta_{\text{amb}} = 25^\circ\text{C}$, and a coolant volume rate of $V_c = 8 \text{ l/min}$

though the thermal resistance consisting of the sleeve and mechanical air-gap is higher (+11.5%). Therefore, no additional rotor cooling effort is necessary. The slightly higher I^2R -losses of the IPMSM with sleeve (+8.0%) result in a higher winding temperature at the applied operating point.

It should be noted, however, that the thermal behavior depends strongly on the losses. In this case, the losses are derived from the sinusoidal current injection. Due to the additional time harmonics of an inverter-fed machine, the losses can be significantly higher, especially depending on the applied switching frequency.

6 Conclusion

The comparison of the rotor concept with buried permanent magnets and carbon fiber sleeve with a state-of-the-art rotor topology leads to the following results:

- High mechanical strength and therefore maximum speed due to carbon fiber sleeve
- High magnet utilization due to low flux leakage despite large total air-gap
- Good field-weakening capability
- Low rotor losses (no segmentation of permanent magnets necessary)
- Low cogging torque and torque ripple under load (no skewing necessary)
- Higher risk of irreversible demagnetization, due to elimination of magnetic stray paths
- Increased manufacturing effort for the production and shrinking of the sleeve as well as the necessary control of the edge effects [15]

Funding Open Access funding enabled and organized by Projekt DEAL.

Open Access This article is licensed under a Creative Commons Attribution 4.0 International License, which permits use, sharing, adaptation, distribution and reproduction in

any medium or format, as long as you give appropriate credit to the original author(s) and the source, provide a link to the Creative Commons licence, and indicate if changes were made. The images or other third party material in this article are included in the article's Creative Commons licence, unless indicated otherwise in a credit line to the material. If material is not included in the article's Creative Commons licence and your intended use is not permitted by statutory regulation or exceeds the permitted use, you will need to obtain permission directly from the copyright holder. To view a copy of this licence, visit <http://creativecommons.org/licenses/by/4.0/>.

References

1. Krings A, Monissen C (2020) Review and trends in electric traction motors for battery electric and hybrid vehicles. 2020 International Conference on Electrical Machines (ICEM), pp 1807–1813 <https://doi.org/10.1109/ICEM49940.2020.9270946>
2. Ito M, Sugimoto S, Takahashi A, Tamiya S (2018) A narrow-bridge rotor to reduce magnetic flux leakage. 2018 XIII International Conference on Electrical Machines (ICEM), pp 1054–1060 <https://doi.org/10.1109/ICELMACH.2018.8507226>
3. Han Z, Yang H, Chen Y (2009) Investigation of the rotor mechanical stresses of various interior permanent magnet motors. 2009 International Conference on Electrical Machines and Systems, pp 1–6 <https://doi.org/10.1109/ICEMS.2009.5382987>
4. Binder A, Schneider T, Klohr M (2005) Fixation of buried and surface mounted magnets in high-speed permanent magnet synchronous motors. Fourtieth IAS Annual Meeting. Conference Record of the 2005 Industry Applications Conference. vol 4, pp 2843–2848 <https://doi.org/10.1109/IAS.2005.1518863>
5. Klohr M (2007) Entwicklung und Konstruktion einer umrichter gespeisten magnetgelagerten Permanentmagnet – Synchronmaschine für 40 kW / 40000 / min (Development and design of an inverter-fed permanent magnet synchronous machine for 40 kW / 40000 / min), Ph.D. Thesis, University of Darmstadt, Darmstadt
6. Baron C (1990) Mechanische Eigenschaften kohlenstoff-faserverstärkter Kunststoffe (CFK) bei Variation der Matrixduktilität und der Bruchdehnung der Fasern (Mechanical properties of carbon fiber reinforced plastics (CFRP) with variation of matrix ductility and elongation at break of fibers). In: Forschungsbericht DLR, Institut für Werkstoff-Forschung Köln
7. Clauer M, Binder A (2022) Automated fast semi-analytical calculation approach for the holistic design of a PMSM in a novel two-drive transmission. 2022 International Conference on Electrical Machines (ICEM), pp 1281–1287 <https://doi.org/10.1109/ICEM51905.2022.9910875>
8. Lu B, Dai N, Xu G, Zhang S, Yang J (2018) Design of the structure of the rotor containment sleeve for high-speed PM machine. 2018 2nd IEEE Conference on Energy Internet and Energy System Integration (EI2), pp 1–5 <https://doi.org/10.1109/EI2.2018.8582028>
9. Wolmarans JJ, van der Geest M, Polinder H, Ferreira JA, Zeilstra D (2011) Composite materials for low loss rotor construction. 2011 IEEE International Electric Machines & Drives Conference (IEMDC), pp 295–299 <https://doi.org/10.1109/IEMDC.2011.5994862>
10. Lee T-W, Hong D-K (2022) Rotor design, analysis and experimental validation of a high-speed permanent magnet synchronous motor for electric turbocharger. IEEE Access

10:21955–21969. <https://doi.org/10.1109/ACCESS.2022.3152525>

11. Soong WL, Ertugrul N (2002) Field-weakening performance of interior permanent-magnet motors. *IEEE Trans on Ind Applicat* 38(5):1251–1258. <https://doi.org/10.1109/TIA.2002.803013>
12. Liu Y (2010) Critical wavelength of eddy currents and its influence on harmonic losses in solid poles. *The XIX International Conference on Electrical Machines—ICEM 2010*, pp 1–6 <https://doi.org/10.1109/ICELMACH.2010.5607999>
13. Valtonen M, Parviainen A, Pyrhonen J (2008) Influence of the air-gap length to the performance of an axial-flux induction motor. *2008 18th International Conference on Electrical Machines*, pp 1–5 <https://doi.org/10.1109/ICELMACH.2008.4800002>
14. Hossain MJ, Shuvo YA, Hossen MM, Kader MA, Islam MZ (2020) Optimization of interior permanent magnet machine embedded with ferrite magnets by varying air-gap and width of permanent magnets. *2020 IEEE Region 10 Symposium (TENSYP)*, pp 929–932 <https://doi.org/10.1109/TENSYP50017.2020.9231014>
15. Grace K, Galoto S, Bodla K, El-Refaie AM (2018) Design and testing of a carbon-fiber wrapped synchronous reluctance traction motor. *IEEE Trans on Ind Applicat* 54(5):4207–4217. <https://doi.org/10.1109/TIA.2018.2836966>

Publisher's Note Springer Nature remains neutral with regard to jurisdictional claims in published maps and institutional affiliations.



Maximilian Clauer, was born in 1993 near Cologne, Germany. He received his Bachelor of Science in Mechanical Engineering and his Master of Science in Automotive Engineering and Transportation from the RWTH Aachen University in 2018 and 2020, respectively. Since 2020 he is with the Institute of Electrical Energy Conversion at the Darmstadt University of Technology as a research assistant. His field of research is electrical machines, especially for automotive application.



Andreas Binder, Senior Member IEEE, Member VDE, IET, VDI, EPE, received the degrees Dipl.-Ing. (diploma) and Dr. techn. (PhD) for Electrical Engineering from the University of Technology, Vienna/Austria, in 1981 and 1988, respectively. Since 1994 he is lecturer (habilitation) at University of Technology, Vienna/Austria, and received in 1997 the ETG-Literature Award of the German Assoc. of Electrical Engineers, VDE. Since October 1997, he is Head of the Institute of Electrical Energy Conversion, Darmstadt University of Technology, as a full professor. He is the author or co-author of more than 350 scientific publications and two books and holds several patents. He received Dr. h.c. from University of Technology Bucharest in 2007 and is the recipient of the Medal of Honour of the ETG/VDE 2009 for outstanding contributions at VDE. Research topics are High-Speed-Motors, Permanent magnet-E-Machines, bearing currents, drive technologies for hybrid and electric cars, drive systems for electric railways, magnetic suspension, magnetic bearings and generator systems.